Quantifying Convective Aggregation Using the Tropical Moist Margin's Length

Tom Beucler[1,2] iD **, David Leutwyler[3]** iD **, and Julia M. Windmiller[3]** iD

[1]Department of Earth System Science, University of California, Irvine, CA, USA, [2]Department of Earth and Environmental Engineering, Columbia University, New York, NY, USA, [3]Max Planck Institute for Meteorology, Hamburg, Germany

Abstract On small scales, the tropical atmosphere tends to be either moist or very dry. This defines two states that, on large scales, are separated by a sharp margin, well identified by the antimode of the bimodal tropical column water vapor distribution. Despite recent progress in understanding physical processes governing the spatiotemporal variability of tropical water vapor, the behavior of this margin remains elusive, and we lack a simple framework to understand the bimodality of tropical water vapor in observations. Motivated by the success of coarsening theory in explaining bimodal distributions, we leverage its methodology to relate the moisture field's spatial organization to its time evolution. This results in a new diagnostic framework for the bimodality of tropical water vapor, from which we argue that the length of the margin separating moist from dry regions should evolve toward a minimum in equilibrium. As the spatial organization of moisture is closely related to the organization of tropical convection, we hereby introduce a new convective organization index (BLW) measuring the ratio of the margin's length to the circumference of a well-defined equilibrium shape. Using BLW, we assess the evolution of self-aggregation in idealized cloud-resolving simulations of radiative-convective equilibrium and contrast it to the time evolution of the Atlantic Intertropical Convergence Zone (ITCZ) in the ERA5 meteorological reanalysis product. We find that BLW successfully captures aspects of convective organization ignored by more traditional metrics, while offering a new perspective on the seasonal cycle of convective organization in the Atlantic ITCZ.

Plain Language Summary The tropical atmosphere tends to be either moist or very dry. This defines moist and dry regions that can be separated using a meandering line, namely the "moist margin." Better understanding the behavior of this "moist margin" would help explain the distribution of tropical water vapor, clouds, and precipitation. Here, we argue that the "moist margin's" length should evolve toward a minimum. By comparing the length of the "moist margin" to a theoretical minimum, we can assess how organized clouds and storms are in the atmosphere: The shorter the "moist margin," the more organized the clouds and storms. This simple rule allows us to better analyze the organization of idealized computer simulations of the tropical atmosphere as well as realistic data sets of the tropical Atlantic's atmosphere.

1. Introduction

The tropical hydroclimate is shaped by deep atmospheric convection, which occurs more frequently in the moist environments of other deep convective updrafts than in dry environments (e.g., Parsons et al., 2000; Peters et al., 2009; Redelsperger et al., 2002; Sherwood, 1999). Deep convection may further moisten its environment through direct effects, such as increased detrainment of cloud water (e.g., K. A. Emanuel & Pierrehumbert, 1996; Holloway & Neelin, 2009; Minschwaner & Dessler, 2004; Sun & Lindzen, 1993), and indirect effects, such as vertical advection of water vapor driven by decreased radiative cooling in the presence of high clouds (e.g., Beucler & Cronin, 2016; Bretherton & Sobel, 2002; Wing & Emanuel, 2014). In unforced simulations of radiative-convective equilibrium (RCE) initialized with a uniform humidity field, this positive feedback, referred to as convective self-aggregation (e.g., Bretherton et al., 2005; Held et al., 1993; Tompkins & Craig, 1998; Wing et al., 2017), leads to the formation and maintenance of anomalously dry and moist regions (Figures 1a and 1c). In the real atmosphere, bimodal probability density functions (PDFs) of upper-tropospheric humidity have long been seen in satellite-based observations of the midlatitudes (e.g., Soden & Bretherton, 1993; Yang & Pierrehumbert, 1994) and the tropics (e.g., Brogniez, 2004; Zhang et al., 2003). Since then, observational progress (e.g., morphological compositing, see Wimmers &
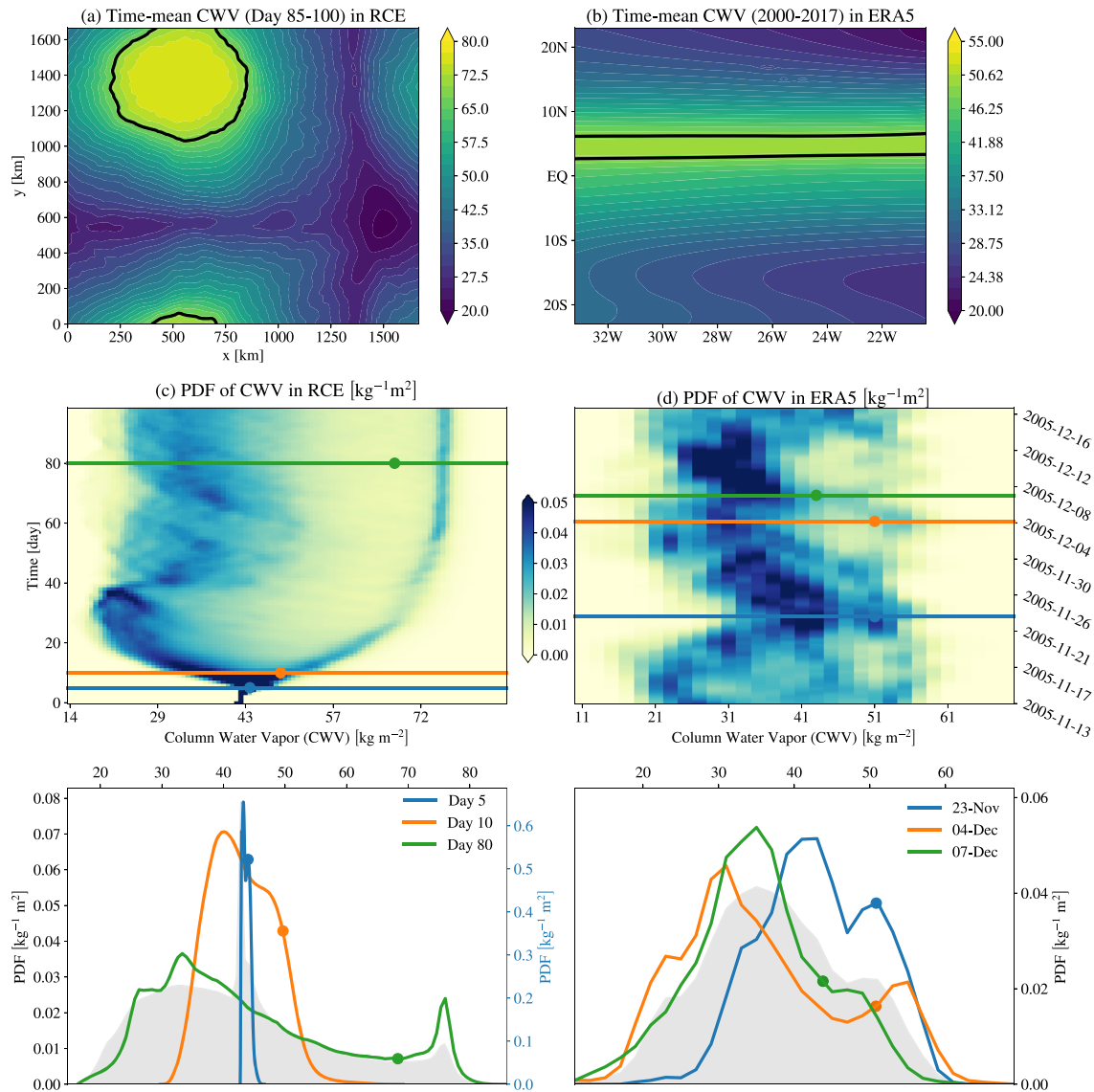
Figure 1. (Top row) Time-mean CWV in units kg m^{-2} for (a) the last 15 days of the 300-K RCE simulation and (b) the ERA5 reanalysis of the Atlantic Intertropical Convergence Zone (ITCZ) over the years 2000–2017. (Middle row) Time evolution of the PDF of CWV for (c) RCE and (d) ERA5 (November–December 2005). For RCE, we denote the 88th percentile of CWV with dots, while we denote the 83rd percentile of CWV with dots for ERA5. (Bottom row) For RCE, we additionally sample the PDFs over 3 different 48-hr time periods. For ERA5, we additionally sample the PDFs over 48-hr windows centered around the dates indicated in the top-right legend. In both cases, we depict the time-mean PDF using gray shading. Note that we do *not* claim that RCE is a good model for the ITCZ despite comparing both to show the versatility of our approach.

Velden, 2011) has confirmed the ubiquity of this bimodality for the full column water vapor (CWV) field (Figure 1d).

Historically, satellite observations led to a *Lagrangian* view of this bimodality, such as the advection-condensation framework (e.g., Beucler, 2016; Pierrehumbert & Roca, 1998; Sherwood, 1996; Sherwood et al., 2006) in which air masses are transported along isentropic surfaces between the Equator and the Poles. Their humidities correspond to the last time air masses reached saturation (the "cold trap," e.g., Pierrehumbert et al., 2007), explaining the dry peak as air masses coming from the Poles and the moist peak as air masses coming from the deep tropics. As the advection-condensation framework ambiguously mixes large-scale dynamics with microphysics, whose spatial scales are separated by ~6 orders of magnitude, systematic analyses of idealized simulations were conducted to better isolate the respective effects of

advection, convection, radiation, and microphysics on water vapor. This led to an *Eulerian* view of this bimodality, in which the formation of large-scale moist and dry regions happens within a week to a month at the ~1,000- to 10,000-km scale through the interaction between CWV and radiation in the slowly rotating tropics (e.g., Beucler et al., 2019; K. Emanuel et al., 2014; Holloway & Woolnough, 2016; C. Muller & Bony, 2015).

Recently, a *mixed Eulerian-Lagrangian* perspective emerged. Mapes et al. (2018) used blended satellite data to identify the 48-mm CWV isoline as a sharp margin (1 mm = 1 kg m^{-2} when used to describe CWV), namely the tropical moist margin (e.g., the black solid line in Figure 1b), separating two spatially coherent regions: the "dry tropics" (dry maximum of the PDF) and the "moist tropics" (moist maximum of the PDF). The CWV distribution of a given air mass can then be inferred from the meandering dynamics of the moist margin, making this new Eulerian-Lagrangian framework (see Masunaga & Mapes, 2020) suitable to both complex observations and idealized simulations (see review by Holloway et al., 2017). These encouraging results, along with the tight link between CWV and convection in the tropics, motivate the central question of our manuscript:

How can we leverage the time evolution of the moist margin to better understand the organization of tropical CWV and convection?

We show that the tropical moist margin's length (MML) can be used to quantify the degree of convective aggregation in both idealized RCE simulations and meteorological reanalysis. We introduce the data sets in section 2. We then generalize the coarsening framework of Craig and Mack (2013) and Windmiller and Craig (2019) to link the CWV's distribution to its time evolution using the moist margin. Based on the coarsening framework, we argue in section 3 that (i) we can diagnose the time evolution of CWV using an empirical potential, an empirical Gibbs free energy, or simply the MML and (ii) the more MML decreases, the more aggregated CWV becomes. Afterward, we derive a simple index exploiting the length of the moist margin to quantify convective aggregation in both idealized simulations and reanalysis in section 4 before concluding in section 5.

2. Data

We analyze two high-resolution data sets with varying degrees of realism and different domain geometries: idealized simulations of RCE on one hand (section 2.1) and high-resolution reanalysis of the tropical atmosphere on the other hand (section 2.2). For conciseness, we do not introduce simulations of intermediate degree of realism and contrast both data sets to illustrate the versatility of our framework rather than compare RCE to observations in details.

2.1. Simulations of Nonrotating RCE

We use the nonhydrostatic limited-area weather and climate model COSMO (Consortium for Small-scale Modeling model, v5.0, Steppeler et al., 2003) in a square, doubly periodic computational domain of 506 × 506 × 74 grid points with horizontal grid spacing of 3 km and use a time step of 30 s. We conduct nine simulations with prescribed uniform sea surface temperatures (SSTs) ranging from 296 to 304 K at 1-K increments. Apart from the size of the computational domain, the configuration follows the RCE-MIP protocol (Wing et al., 2018). As defined in the protocol, each simulation is initialized with a typical tropical profile obtained from a small-domain RCE simulation and run to stationarity (100 days). The reader interested in the details of the numerical model is referred to Appendix A.

In three-dimensional, cloud-resolving simulations of nonrotating RCE, the CWV field evolves from an initially horizontally homogeneous state into distinct, spatially coherent, dry and moist regions (Figure 1a) that map to a bimodal distribution (Figure 1c). Qualitatively, the presented simulations evolve similarly to other unforced simulations of RCE (see, e.g., for a review Wing et al., 2017). A peculiar aspect of the present simulations is that they do not exhibit a dry bias (e.g., end of section 3.3 from Holloway et al., 2017). In contrast to typical limited-domain RCE simulations, the dry mode of the CWV PDF is centered around 32 kg m^{-2}, which compares well to the CWV distribution observed in the tropical Atlantic (see Figure 1d). Note that repeating the presented simulations on a computational domain using 206 × 206 × 74 grid points results in a drier domain-mean profile (not shown). However, compared to the CWV climatology in the Atlantic, the moist mode has much larger CWV values.

2.2. Reanalysis of the Atlantic Intertropical Convergence Zone

As a step toward understanding convective aggregation in the observed atmosphere, we complement the idealized simulations of RCE with meteorological reanalysis of the Atlantic Intertropical Convergence Zone (ITCZ).

We choose the European Centre for Medium-Range Weather Forecasts Reanalysis version 5 (ERA5), which was produced by assimilating observational data in version CY41R2 of the Integrated Forecast System (Hersbach et al., 2020), for its high spatiotemporal resolution and realistic hydrologic cycle. This new reanalysis has a spatial grid of $0.25° \times 0.25°$, which resolves some deep convective events and allows us to capture the moist margin's curvature. Furthermore, it has a temporal resolution of 1 hr, allowing us to accurately sample the atmospheric energy budget over periods as short as 48 hr. The analysis period is defined as the 1 January 2000 until the 31 December 2017. To focus on the Atlantic ITCZ, we restrict our analysis to the domain between latitudes of 23°S and 23°N (the standard definition of the tropics) and extending from longitudes of 34°W to 14°W. The domain, depicted in Figure 1b, is located between the moistest regions of South America and Cape Verde, and excludes land areas.

The defined Atlantic domain is characterized by the very moist ITCZ and by the much drier subtropics alike (Mapes et al., 2018). These two regions differ distinctly in their CWV, as illustrated by the multiyear time average of the CWV field, which exhibits a region of high CWV that zonally spans the domain (moist tropics), and a comparatively dry region surrounding it (subtropics); see Figure 1b. The separation of the domain into dry and moist regions is also evident in the CWV distribution, which is characterized by two modes (Figure 1d). Its evolution displays alternating phases in which the PDF either becomes more unimodal or more bimodal. These different phases will be discussed in detail below.

3. Theory

Motivated by the results of self-aggregation studies, the key premise of this paper is that the degree of convective aggregation is reflected in the bimodality of the CWV distribution, with a more pronounced bimodality corresponding to a higher degree of aggregation. Although three-dimensional simulations of RCE, satellite observations, and reanalysis data sets display a bimodal distribution of CWV (Figures 1c and 1d), a *physical mechanism* unambiguously explaining this bimodal nature remains to be identified. In particular, testing hypotheses established using the RCE framework on observational data sets remains difficult as we lack analysis frameworks applicable to both. Thus, we here aim at developing a flexible yet simple framework relating the CWV's distribution to its time evolution. Our theoretical framework is motivated by an analogy between the time evolution of the tropical atmosphere's moist and dry regions and a phase separation process. We introduce this analogy (section 3.1), develop a flexible framework relating the CWV's distribution to its time evolution (sections 3.2 and 3.3), and finally demonstrate that this relation can be described using a *single variable*, namely the MML (section 3.4).

3.1. A Phase Separation Analogy

The analogy is that in the tropical atmosphere, moist and dry regions separate in a way similar to oil and water. Starting with a system that contains oil and water molecules, will the equilibrium state be a homogeneous mixture or two separate phases? At constant temperature and pressure, the equilibrium state minimizes the Gibbs free energy (G), which is the maximum amount of nonmechanical work that can be extracted from a closed system. In the case of an idealized mixture of oil and water, G helps explain why the homogeneous mixture state is only favorable for temperatures far above the boiling temperature of water (e.g., Schroeder, 2000, p. 190).

According to the Landau theory of phase transitions, G can be written as the sum of (1) a term only depending on state variables (e.g., temperature and pressure) and (2) a potential V depending on a so-called "order parameter." In the case of an idealized oil and water mixture, the "order parameter" may be the oil concentration calculated within a finite mixture volume. For a fixed thermodynamic state, G only depends on the order parameter, and this dependence can be entirely described using V: If the potential has two minima (*double-well* potential), the equilibrium state will be two unmixed phases, while it will be a homogeneous mixture if the potential only has one minimum (*single-well* potential).

For a closed system, the second law of thermodynamics implies that G monotonically decreases in time until the system reaches the state of minimal G, that is, the equilibrium state. In the case of a double-well potential describing an oil and water mixture, G monotonically decreases as oil and water separate. The order parameter's time evolution is then given by the so-called time-dependent Ginzburg-Landau equation. In the case of a well-mixed but out-of-equilibrium system, this evolution is referred to as coarsening, which, for example, describes the formation and growth of isolated patches of oil and water in a salad dressing. One caveat, which will become important in our discussion of the ITCZ reanalysis data below, is that in the case of an open system, G can also change via advection through the system's boundaries. Keeping this caveat in mind, we henceforth develop our theoretical framework using the closed RCE simulations before applying it to the ITCZ reanalysis.

3.2. Potential

Motivated by the well-resolved self-aggregation of convection and the corresponding broadening of the CWV distribution in our idealized RCE simulations, we start by asking the question: Why do anomalously moist and dry regions dry or moisten further?

While several physical mechanisms supporting such a development have been formulated (Beucler et al., 2018; Bretherton et al., 2005; K. Emanuel, 2019; K. Emanuel et al., 2014; Tompkins, 2001), Windmiller and Craig (2019) show that these different mechanisms may all lead to similar upscale growth of moist and dry regions as long as humidity anomalies are locally reinforced. Whether local humidity anomalies are reinforced can be conveniently investigated by first making the following assumption: *The time evolution of CWV, described by its local time derivative ∂_tCWV, only depends on CWV*. In other words, we study how fast values of CWV increase or decrease, assuming that for a given CWV the sign and rate only depend on the CWV value itself. In this case the CWV local time derivative (CWV tendency for short) can be described by a function f(CWV) that only depends on CWV:

$$\frac{\partial \mathrm{CWV}}{\partial t} = f(\mathrm{CWV}). \tag{1}$$

Following section 3.1 and Windmiller and Craig (2019), we express f(CWV) as the gradient of a (Landau) potential in CWV space, that is,

$$\frac{\partial \mathrm{CWV}}{\partial t} = f(\mathrm{CWV}) = -\frac{d V(\mathrm{CWV})}{d \mathrm{CWV}}. \tag{2}$$

Under this assumption, the time evolution of the CWV field is entirely determined by its potential, which describes the system's ability to stabilize by changing CWV. Provided with the potential V(CWV), the question of whether local humidity anomalies are reinforced can then be addressed by investigating the shape of the potential.

There are, in principle, two ways to investigate the shape of the potential. On one hand, we can start from physical principles and attempt to *derive the potential* (or forcing function f(CWV)), as has been the focus of numerous previous studies (e.g., Bretherton et al., 2005; Craig & Mack, 2013; K. Emanuel et al., 2014). On the other hand, we can directly use the data to *diagnose the potential*, which is the approach we pursue in this work. To this end, we calculate an empirical potential for a given time period and domain by first conditionally averaging all CWV tendencies (independently of time and location) based on their respective CWV content to obtain f(CWV) and by then integrating Equation 2 with respect to CWV:

$$V(\mathrm{CWV}) \approx -\int_{\mathrm{CWV}_0}^{\mathrm{CWV}} \mathbb{E}\left(\frac{\partial \mathrm{CWV}}{\partial t}\bigg|\widetilde{\mathrm{CWV}}\right) d\widetilde{\mathrm{CWV}}, \tag{3}$$

where CWV_0 is an arbitrary constant fixing the gauge of the potential so that $V(\mathrm{CWV}_0) = 0$ and $\widetilde{\mathrm{CWV}}$ is an integration variable. It is important to note that Equations 1 and 2 are approximations, as in reality the tendencies of CWV may depend on more than just CWV itself. By assuming that the evolution of CWV is given by its mean value in CWV space, we successfully capture the time evolution of the
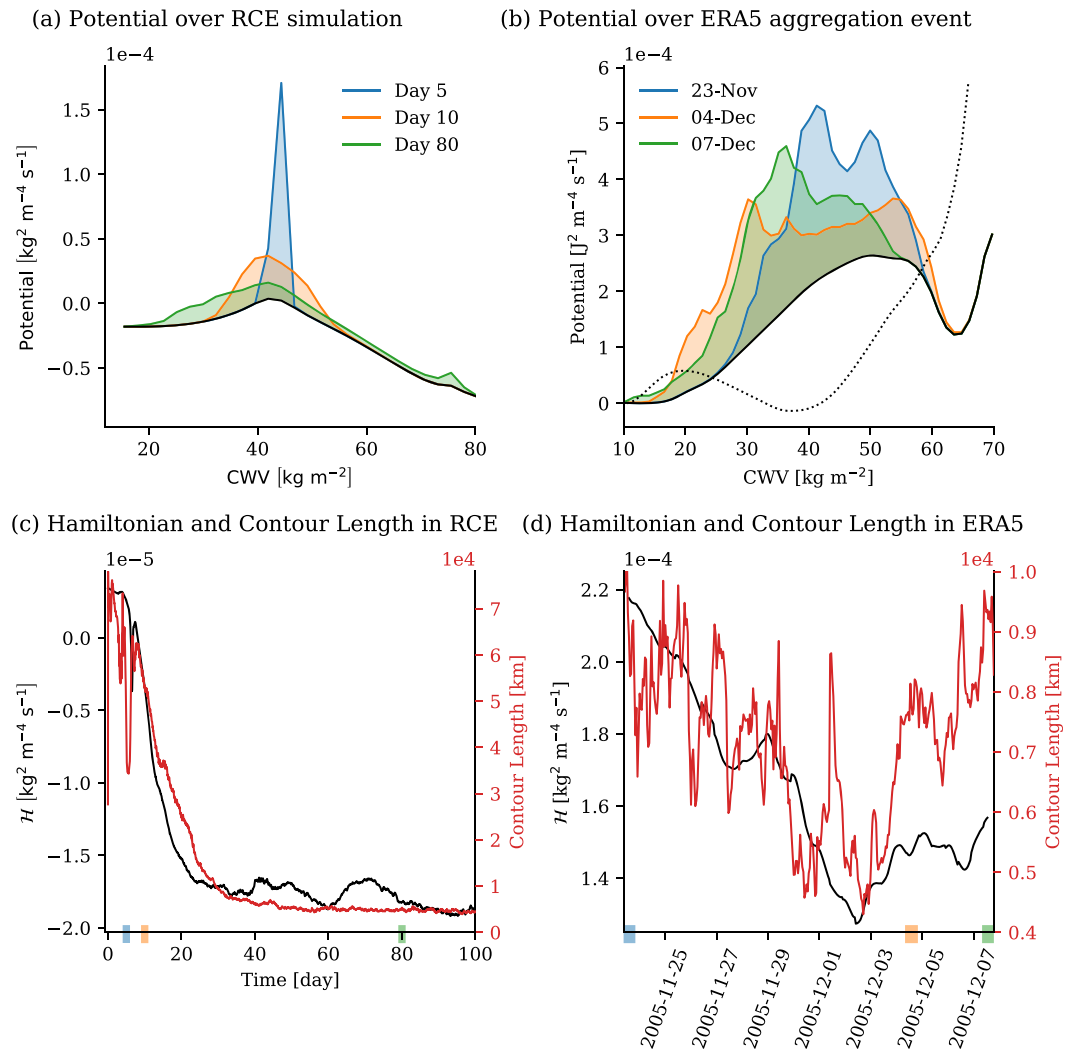
Figure 2. (a) Potential calculated from the CWV tendency in RCE (black line) and PDF of CWV sampled over three different time periods (the shading indicates the sum of the potential and the PDFs, multiplied by a constant for visualization purposes). (b) Potentials calculated from the CWV tendency from ERA5 between 23 November 2005 and 4 December 2005 (solid black line) and between 4 December 2005 and 7 December 2005 (multiplied by a factor of 0.5, dotted black line) and PDF of CWV sampled over 48-hr windows centered around the dates indicated in the top-left legend (shading). (c) Empirical Gibbs free energy (black line) and contour length (red line) versus time for RCE. (d) Empirical Gibbs free energy (black line) and contour length (red line) versus time for ERA5. The time periods used in (a) and (b) are marked with colored shading in (c) and (d).

spatial-mean CWV field but reduce the spatial variance of the CWV time tendencies by a factor ~100 (as estimated using the Beucler et al., 2019, framework, not shown). Finally, note that it is possible to choose column moist static energy (MSE) instead of CWV as the order variable in Equation 2: In that case, Equation 3 can be applied to the MSE tendencies of individual physical processes, which helps link our framework to the MSE budget framework extensively used by the self-aggregation community (see Appendix B for more details).

We are now in a position to use the two data sets described in section 2 to illustrate how the shape of the potential can help us understand the time evolution of the CWV distribution and therefore yield insight into the amplification of humidity perturbations in the tropical atmosphere. We start by discussing the potential and time evolution of the CWV distribution for an idealized RCE simulation with a prescribed SST of 300 K (Figure 2a).

We calculate the potential according to Equation 3 using the hourly tendencies of CWV over the 100 simulation days and 30 CWV bins. Its analysis reveals a double-well potential, that is, a local maximum which separates two potential minima from each other. According to Equation 2, the potential dictates the tendency for a given CWV to "roll down" toward the potential minimum and predicts faster moistening or drying for a steeper gradient. In the case of the presented double-well potential, the CWV content of atmospheric columns containing CWV values larger than the local maximum of the potential is predicted to increase, while the CWV content of atmospheric columns containing CWV smaller than the local maximum of the potential is predicted to decrease. CWV will continue to evolve until atmospheric columns reach the local minimum of the potential at the moist or dry ends of the CWV range. Note that it is difficult to determine the exact location of the two potential wells from Figure 2a, which reflects challenges in sampling a potential minimum using Equation 3. This sampling issue arises because the evolution of CWV toward the two minima becomes increasingly slow the closer the CWV gets to the potential minima as the gradient of the potential and hence the rate of moistening and drying go to zero (see Equation 2). As a result, the two potential's local minima are calculated from a relatively small number of data points. However, despite the challenge of resolving the two potential's minima, the existence of a well-resolved potential maximum for a CWV value CWV_{max} indicates moistening of CWV values larger than CWV_{max} and drying of CWV values smaller than CWV_{max}, as shown in Figures 2a and 2b. Hence, a well-resolved potential maximum is sufficient to diagnose bistability as moistening and drying are physically limited by the positive definition of CWV (lower bound of 0) and condensation of water vapor into liquid and ice (upper bound given by the saturation CWV).

The evolution of CWV diagnosed by the potential compares very well with the time evolution of the CWV distribution shown in Figure 1c. This close link can be conveniently visualized by adding the CWV distributions shown in Figure 1c to the potential. As the potential predicts that a given CWV content evolves either to the moist or dry potential minimum depending on its position relative to the potential maximum, the CWV distribution is expected to fill up the two potential wells with time. Starting from a CWV distribution which initially peaks at the potential maximum, we can see the two wells being filled up in Figure 2a.

Unlike in RCE simulations, CWV in the tropical Atlantic does not monotonically evolve toward a stationary state as it is continuously forced by CWV advection through all of the domain's boundaries. As a consequence, its CWV distribution can only be considered bimodal in the long-term time average (see gray shading in Figure 1d), while it frequently also appears to be unimodal on ~1-week timescales (e.g., see Figure 1d). This motivates us to split the CWV evolution into periods evolving toward a more bimodal CWV state ("aggregating" phases) and periods evolving toward a more unimodal state ("disaggregating" phases).

Repeating the analysis for a 2-week period (from 23 November 2005 to 7 December 2005) in the tropical Atlantic shows a clear relationship between the "aggregating" phase of CWV and its potential (Figure 2b). We have deliberately chosen this 2-week period using the spatial variance of CWV so that it contains an aggregating phase (from 23 November to 4 December) followed by a disaggregating phase (from 4 December to 7 December). In the first phase, the distribution widens considerably and appears to fill up the two potential wells, similar to the evolution observed in RCE. In the subsequent disaggregating phase, the system dries and the evolution does not follow the double-well potential (drying of the moistest CWV and moistening of the driest CWV) anymore. The corresponding potential from the tendencies of the disaggregation phase (dotted black line in Figure 2b) shows that, apart from a weak drying tendency for the extremely dry columns, all CWV values are predicted to evolve toward a single potential minimum around 40 kg m^{-2}. In contrast to the aggregating phase, the disaggregating phase is therefore more closely described by a single- rather than a double-well potential.

To summarize, using Equation 3 to calculate an empirical potential from the CWV tendencies provides a simple approach to assess the time evolution of the CWV distribution. In particular, we have shown that the CWV distribution is expected to evolve toward a more bimodal distribution, with moistening of the moist and drying of the dry regions, if the associated potential has a double-well shape. Can we exploit these findings to define aggregating and disaggregating phases more formally?

3.3. Gibbs Free Energy

The double-well structure of the potential in idealized simulations of RCE suggests defining the degree of aggregation of a given CWV distribution as the degree to which the PDF of CWV has "fallen" into the two

potential wells, which we calculate by taking the spatial-mean $\langle \cdot \rangle$ of the potential field $V\left[\mathrm{CWV}(t,\ \vec{x})\right]$ over the spatial domain $\mathscr{D}$:

$$G(t) \stackrel{\mathrm{def}}{=} \left\langle V\left[\mathrm{CWV}(t,\ \vec{x})\right]\right\rangle_{\mathscr{D}}. \tag{4}$$

Expressed in words, G, at a given time, is the domain average of the empirical potential calculated from the CWV field. G therefore quantifies the energy of a given configuration of the CWV field, and we refer to G as the Gibbs free energy (or energy function) of our system in reference to the analogy in section 3.1. Note that the Landau free energy defined by Equation 2 of Windmiller and Craig (2019) is a special case of the Gibbs free energy defined here, as the Landau free energy makes the additional assumption that all horizontal transport can be described by small-scale mixing, for example, Fickian diffusion.

The time evolution of G only depends on the time evolution of the CWV field. For instance, during an aggregating phase (i.e., during a phase in which the potential has a double-well shape), G decreases as long as the CWV field becomes more bimodal. It is interesting to note that if the time evolution of the CWV field were exactly described by Equation 2, with a given potential function $V(\mathrm{CWV})$ fixed in time, G would have to monotonically decrease in time. This can readily be shown by taking the time derivative of Equation 4 (see also, e.g., Krapivsky et al., 2010):

$$\frac{dG}{dt} = \left\langle \frac{dV}{d\mathrm{CWV}}\frac{\partial \mathrm{CWV}}{\partial t}\right\rangle_{\mathscr{D}} \stackrel{(\text{Equation 2})}{=} -\left\langle \left(\frac{dV}{d\mathrm{CWV}}\right)^2\right\rangle_{\mathscr{D}} \leq 0, \tag{5}$$

where, in the first step, we have applied the chain rule and in the second step used Equation 2 to replace $\partial_t\mathrm{CWV}$ with the potential's gradient in CWV space. Note that Equation 5 predicts opposite time evolutions for the CWV distribution depending on whether the potential is bimodal or unimodal, that is, whether we are in an aggregating or a disaggregating phase. In the case of a bimodal potential, G is minimized by the moistening of moist and drying of dry regions while in the unimodal case G is minimized by the moistening of dry and drying of moist regions. The monotonic decrease of G predicted by Equation 5 is, however, conditional on the time evolution of the CWV field being exactly captured by Equation 2. This in turn means that in a system where Equation 2 applies only approximately, as expected for the RCE simulations and the reanalysis data here, the time evolution of G provides an indication of how well a given potential describes the time evolution of the CWV field. In particular, periods during which G increases indicate that the CWV field is not adequately described by Equation 2 during these periods. Note, however, that in the case of an open system, for example, in the reanalysis data, G can also increase via advection through the boundaries (see section 3.1).

The time evolution of G for the RCE simulation and the reanalysis is shown in Figures 2c and 2d, respectively. In the RCE simulation, G rapidly decreases with time for about 40 days. After the initial rapid minimization, the decrease in G slows down, until it ultimately starts oscillating around a new stationary state. As discussed in more detail below (section 4), the decrease in G with time matches the increasing degree of aggregation in the RCE simulation. We also note that while the weak oscillation in G during the later stages of self-aggregation cannot be explained within our framework (see Equation 5), they are reminiscent to oscillations previously seen in self-aggregation studies and discussed in detail by Patrizio and Randall (2019). In contrast to the RCE simulation, the time evolution of G in ERA5 reanalysis is not as monotonic (Figure 2b), but the two phases described above can still be clearly identified. In the first phase (aggregation phase, 23 November to 4 December), G decreases rapidly, and the CWV distribution becomes more bimodal. Note that the most bimodal state has a time lag of about 2 days with respect to G's minimum. After reaching its minimum value on 2 December, G starts slowly increasing again, indicating that the CWV distribution is forced by a different potential that favors unimodality during the disaggregating phase (see, e.g., Figure 1b).

It is important to note that while we use the time evolution of G to diagnose when an equilibrium state is reached, we cannot use it to predict this equilibrium state's properties. According to Equation 5, a minimization of G implies that the equilibrium state is only reached once the domain is either entirely moist or entirely dry, depending on whether the moist or dry potential well is deeper. However, this state might not be accessible because it violates energy or mass conservation. For example, isolated systems like

doubly periodic RCE simulations cannot have entirely dry (and therefore nonprecipitating) equilibrium states as they would violate energy conservation: Convective heating would be zero while radiative cooling would be nonzero. Additional constraints are required to make predictions about the final equilibrium state, such as the fractional area σ of the domain in the moist and dry phases. We refer the interested reader to Lorenz et al. (2005), Craig (1996), and Craig and Mack (2013) for simple σ scalings from mass and energy conservation and to Rennó and Ingersoll (1996) for a historical σ scaling that additionally models atmospheric convection as a heat engine.

In summary, our results suggest that for RCE simulations, the empirical Gibbs free energy G can diagnose the time evolution of the degree of aggregation quite well. For more realistic conditions, G captures the aggregating and disaggregating phases, establishing a clear relation between G and the modality of the CWV distribution. Although G and CWV tendencies do not covary perfectly, the results are encouraging enough to simplify the analysis further.

3.4. Moist Margin's Length

The empirical Gibbs free energy introduced above successfully diagnoses the degree of aggregation as the CWV distribution becomes bimodal. However, employing that diagnostic entails defining and calculating the full potential function, which requires ~1 week of hourly data. To further simplify our analysis, we aim to introduce a simple diagnostic variable that only requires a snapshot of the CWV distribution.

For this purpose, we leverage a surface tension argument based on the analogy discussed in section 3.1 and argue that under the *assumption of a strictly continuous CWV field*, G's tendency is correlated with the length of the contour orthogonal to the gradient separating moist from dry regions, namely the moist margin (see section 1). Analogous to the surface tension at the interface between water and air, which results from the larger attraction of water molecules to other water molecules rather than dry air molecules, the aggregation of moist regions may result from the increased likelihood of deep convection to occur in the moist environment of other deep convective updrafts rather than in the drier surroundings. The net effect of this attraction between deep convective updrafts is an inward force at the boundary of the moist tropics which acts to minimize the length of its contour, that is, the MML. The main point of this analogy is that a surface tension-like effect can result from the local reinforcement of humidity perturbations. Here, we investigate when, rather than why, humidity perturbations amplify and hypothesize that a surface tension-like effect acts during "aggregating" phases, that is, during times of a double-well potential.

To better apprehend the link between G and MML, it is useful to understand how the atmosphere minimizes G during aggregation: Initially, G can be reduced by letting dry locations dry further (rolling down into the dry potential well) and moist locations moisten (rolling down into the moist potential well). A local drying and moistening would ultimately result in a spatially random field containing only dry and moist locations, each at the very bottom of the potential well. However, a strictly continuous field that spans across the two potential wells must always contain values in between, or it would not be continuous. Minimizing G thus entails reducing the number of values on the potential hill as much as possible. In a continuous field, G can thus only fully minimize after the local moist (or dry) patches merge. Combining the respective patches allows further reduction of the number of locations on the potential hill since fewer values are needed between the wells. Ultimately, the system should end up in a state with a single CWV minimum, a single CWV maximum, and a margin separating the two, orthogonal to a strong CWV gradient. Since the CWV value at the margin will always fall on the potential hill, estimating the length of the moist margin and its tendency from the CWV distribution should thus serve as an analog diagnostic to G. In practice, the moist margin does not necessarily need to reside exactly on the peak of the potential hill, but at least, it will reside "somewhere" on the hill.

To estimate the MML from data, we proceed in three steps. First, we define the moist margin using a fixed percentile of the CWV distribution (e.g., the 88th CWV percentile in RCE, representing the antimode of the CWV distribution of the last 15 days; see Appendix C for details). Choosing a fixed percentile allows the areas of the moist and dry regions to remain steady (assuming constant grid cell area) while the contour can freely evolve in time. This is advantageous for testing the idea of surface tension which, for a given area, predicts that the contour length evolves toward the minimal possible length determined by the area. Second, we use this moist margin to define a mask separating the dry regions (0) from the moist regions (1). Third, we

measure the total contour separating zeros from ones using the measure module from the scikit-image library version 0.15.0 (Van der Walt et al., 2014) in Python version 3.7.3 (e.g., Sanner et al., 1999), subtract the contours at the domain's edges to avoid double counting of spatially periodic regions, and multiply the result by the grid size to convert it to metric units. As a result, we can efficiently calculate MML at each time step from a snapshot of the CWV field and the sole knowledge of the CWV percentile. Here, we choose the antimode of the bimodal CWV PDF as our CWV percentile, that is, the local minimum between the two CWV maxima. Calculating this local minimum yields the 88th percentile for RCE and the 83rd percentile for ERA5.

We can now test the relationship between G and MML by comparing their evolution in RCE simulations and ERA5 reanalysis (Figures 2c and 2d). For RCE, we find that the MML systematically decreases in time and that there is a close (but not perfect) correlation between the time evolution of G and the MML (correlation coefficient of 0.90). The correlation indicates that instead of G, we can also use the MML to measure the degree of aggregation. For ERA5 reanalysis, the time evolution of the MML is comparatively noisy, but it can still be divided into two periods. In particular, the MML shows an overall decrease during the aggregating phase in which G decreases (correlation coefficient of 0.47) and an overall increase during the disaggregating phase in which G increases (correlation coefficient of 0.64). These correlations of ∼0.5 demonstrate that the link between G and the MML is not as simple for externally forced, open systems such as the real tropics, where the time evolution of G and the MML cannot be related via a single surface tension constant. From a different perspective, the fast timescale of the MML's rapid oscillations and the slow timescale of self-aggregation are separated by a factor ∼20 in RCE but only by a factor ∼10 in ERA5 (see Appendix D for details), contributing to the weaker correlation between G and the MML for ERA5. Nonetheless, the timescale separation and coevolution of G and the MML suggest that we can measure the degree of aggregation by measuring the MML, motivating the development of a new index for convective aggregation in the next section.

4. Application to Idealized Simulations and Reanalysis

So far, we have hypothesized that processes exist which make the tropical atmosphere bistable with respect to its humidity content and thus act to establish the bimodal nature of CWV in the tropics. In particular, we have outlined how this bistable nature can be understood in terms of a double-well potential and how the replenishment of the potential wells relates to changes in the corresponding energy of the system (G). The observation that the tendency of G correlates well with the tendency of the length of the contour separating dry and moist areas (MML) has led us to propose the MML as a diagnostic for convective aggregation. Below, we illustrate how these ideas can be used to relate changes in the CWV distribution to changes in contour length. To this end, we make use of our two data sets: three-dimensional RCE simulations (section 4.2) and the Atlantic ITCZ (section 4.3). The latter is more complex as the RCE simulation depicts an idealized representation of the tropics using homogeneous boundary conditions and no planetary rotation on a square domain. This difference between the two systems is addressed by developing two distinct yet consistent definitions of the minimum contour length (section 4.1).

4.1. Definition of the BLW Index

Based on the ideas outlined in sections 3.3 and 3.4, we introduce a new index to measure the degree of aggregation of a given CWV distribution. The key idea of the index is that aggregation leads to a shortening of the MML, that is, the total length of the contours surrounding the moist regions.

In general, the index is defined as

$$\mathrm{BLW} \stackrel{\text{def}}{=} \left(\frac{\text{Minimal Contour}}{\text{MML}} \right), \tag{6}$$

where we compare the MML to the Minimal Contour, that is, the minimal length the contour could have for an assumed underlying shape of the moisture field. As illustrated in Figure 3, an index BLW = 1 indicates that the moisture field adopts the exact underlying shape of minimal contour. In contrast, BLW = 0 corresponds to the limit of an infinitely long moist margin, either because there is an infinitely large
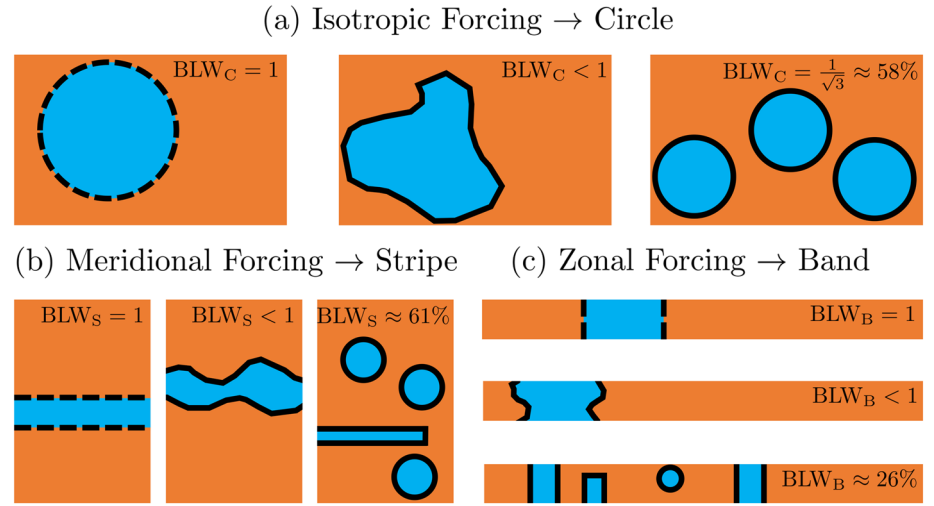
Figure 3. BLW for idealized convective clusters (light blue shapes) in a drier environment (orange background) for three different moisture forcing scenarios leading to three distinct shapes of minimal contour (dashed black lines): (a) Isotropic forcing leading to a circle, (b) meridional forcing leading to a zonally oriented stripe, and (c) zonal forcing leading to a meridionally oriented band.

number of small moist clusters or because the contour is non-rectifiable, that is, "fractal-like." Intermediate values of BLW correspond to a "deformed" contour or a finite number of moist clusters.

For doubly periodic RCE simulations on square computational domains, the minimal contour depends on the fraction of the domain covered by the moist region. As outlined by Holloway and Woolnough (2016), if the moist region covers less than about one third (more precisely $100/\pi$ percent) of the domain, the minimal contour MML is obtained when the moist region is organized in the shape of a single circle of radius Minimal Contour/(2π) and area $\mathscr{A}$, yielding the "circle" version of our index (Figure 3a):

$$\mathrm{BLW_C} \overset{\text{def}}{=} \frac{2\sqrt{\pi \times \mathscr{A}}}{\mathrm{MML}}. \tag{7}$$

The moist area ($\mathscr{A}$) is defined as the total area of the grid points exceeding the CWV threshold used to define the moist margin. To define the moist margin, we use a temporally fixed percentile of the CWV PDF: the 83rd percentile for ERA5 and the 88th percentile for RCE (see Appendix C for details). A notable advantage of using a percentile-based approach instead of an absolute threshold such as $48\,\mathrm{kg\,m^{-2}}$ is that it maintains a constant area for the wet and dry regions during the simulation's evolution and across the nine prescribed SSTs. In other words, the rank in the CWV distribution (and thus the area of the moist region) is fixed, while the threshold magnitude in units $\mathrm{kg\,m^{-2}}$ changes as the simulation evolves, allowing us to meaningfully compare the degree of aggregation across SSTs.

In contrast to the RCE simulations discussed above, the presence of a meridional SST gradient in the tropics externally organizes deep convection into the tropical rain belts. The predominantly zonal orientation of the tropical rain belt in the Atlantic is reflected in the zonal orientation of the moist region (see, e.g., Figure 1b). In that case, the minimal contour MML is obtained when the moist region is a single zonal stripe of length MML/2, yielding the "stripe" version of our index (Figure 3b):

$$\mathrm{BLW_S} \overset{\text{def}}{=} \frac{2 \times L}{\mathrm{MML}}, \tag{8}$$

where L is the length of the considered domain. In the particular case of the Atlantic stripe, this length is approximately 2,200 km, where we have approximated the $1° \times 1°$ longitude-latitude grid from ERA5 as a locally Cartesian $110\,\mathrm{km} \times 110\,\mathrm{km}$ grid.

In the common case where wind shear organizes convection into "bands" orthogonal to the wind shear vector, namely squall lines and arcs (e.g., Robe & Emanuel, 2001; Rotunno et al., 1988), the "stripe" version of

our index can be generalized to take into account the forcing's orientation. For example, long-channel simulations of RCE typically develop strong zonal wind shears (e.g., Posselt et al., 2012; Wing & Cronin, 2016) that organize moist regions into meridional bands, motivating the "band" version of our index (Figure 3c):

$$\text{BLW}_\text{B} \overset{\text{def}}{=} \frac{2 \times \ell}{\text{MML}}, \tag{9}$$

where ℓ is the width of the considered domain.

Before applying BLW to our two data sets, we remind the reader that BLW only relies on two explicit assumptions in *all* cases: (i) the CWV threshold used to define the moist margin and (ii) the underlying moisture shape of minimal contour. These two assumptions make BLW values easy to interpret (Figure 3), especially when choosing the "default" values of the two assumptions: (i) the CWV PDF maximum if the PDF is unimodal and its antimode if the PDF is bimodal and (ii) a circle if the forcing is isotropic or its direction unknown. For comprehensiveness, we finish this section by noting two corner cases that require adapting assumption (ii) and hence the definition of BLW. In the isotropic case, if the moist area occupies most of the domain, then the reference circle shape may be more appropriate for the dry than the moist region, in which case $\mathscr{A}$ in Equation 7 must be replaced with the total area of the grid points *below* the CWV threshold used to define the moist margin. In the anisotropic case, if there are not enough grid points exceeding the CWV threshold to form a moist stripe extending across the domain, then it might be more appropriate to assume a different reference moisture shape, for example, a circle.

4.2. Idealized Simulations of RCE

In the first few days of the simulation, the distribution of CWV is strongly peaked on top of the local potential maximum (see blue line in Figure 2a). As soon as the first convective cells form, self-aggregation starts acting on the moisture field (negative G tendency accelerates after Day 11, Figure 2c) and the CWV distribution quickly becomes bimodal (Figure 1c). During this phase, a dry maximum can be identified around 32 kg m^{-2} and a moist maximum around 55 kg m^{-2}. In the subsequent phase, the dry (or first) maximum remains at a constant value, while the moist (or second) maximum moves to beyond 70 kg m^{-2}. Qualitatively, the development into a bimodal distribution appears robust across the nine simulated SSTs (see Appendix C). However, at warmer SSTs, the maxima of the two modes are further spaced apart. For example, the maxima are located at 33.2 and 75.9 kg m^{-2} at 300 K and at 33.9 and 111.9 kg m^{-2} at 304 K (Figure 4h).

The ratio of the dry to moist mode appears constant, despite the moist mode rapidly moving to larger CWV values and becoming less peaked with increasing SSTs. More specifically, the minimum separating the two modes remains at the 88th percentile of the CWV distribution (see dots in Figure 4h); that is, the moist mode constantly covers about 1/9th of the computation domain. Here, we exploit this property to empirically define a contour dividing the domain into a dry and a wet area (see section 4.1).

Obtaining that contour allows for a spatial, object-oriented perspective of the simulation's evolution (Figures 4a–4e): After the initial set of convective cells have formed, many small cells of high moisture content quickly coalesce into increasingly larger clusters. As they coalesce (Days 11–30), the eccentricity of the largest object steadily increases, indicating that the clusters become increasingly asymmetric (until Day 30; see Figure 4g). Once only a few clusters remain, the eccentricity starts to decrease (i.e., the clusters become more circular), until they merge into a single cluster around Day 54. Note that the merging process of the two last clusters leads to the transient formation of a very elongated cluster which can be seen as a sudden increase in eccentricity around Day 54. During the next 10 days, the final cluster becomes more circular until its shape becomes stable around Day 65.

The described evolution appears well captured by BLW$_\text{C}$ (Figure 4f). Between Days 11 and 46, the overall contour length is rapidly shortened by the small moist cells coalescing, and thus, the index increases rather quickly. During the middle period (Days 46–65), the rate of change in BLW$_\text{C}$ slows down, as the contour is then mainly shortened by spatial rearrangement of moisture toward a circular shape. In the final equilibrium phase, the value of BLW$_\text{C}$ remains rather constant. Note that although the cluster at Day 99 (Figure 4e) appears quite round, BLW$_\text{C}$ only achieves a value of about 0.4, indicating that, at the considered timescales, the obtained contour remains more than twice as long as that of a perfect circle with the same area. Applying a 20-day running mean results in a CWV field similar to that displayed in Figure 1a, and a
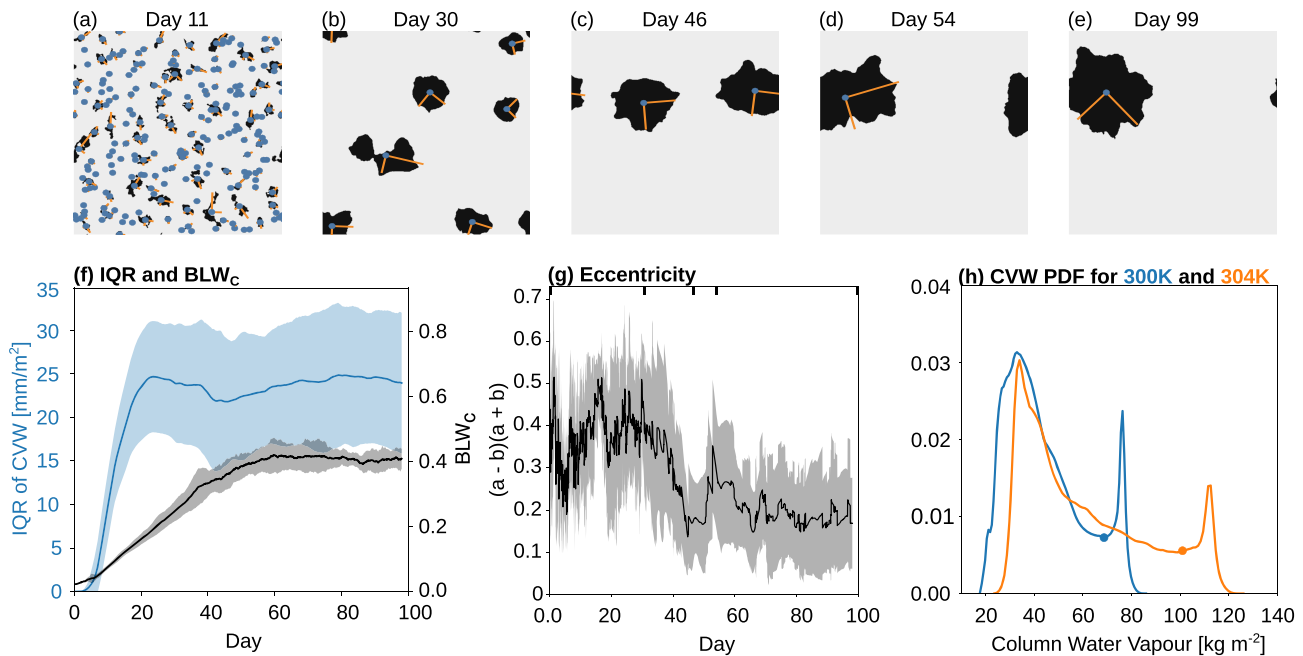
Figure 4. Evolution of CWV and aggregation diagnostics in a set of nine RCE simulations with varying SSTs (296–304 K, depicted by the shading in f and g), after applying a 48-hr temporal mean. (a–e) Snapshots of high and low CWV in the 300-K simulation: The black mask identifies grid points above the 88th percentile of CWV. The blue dots mark the centroids of connected grid points, and the orange lines the respective principle axis. (f) BLW_C (black) and CWV interquartile range (blue). (g) Eccentricity of the largest object (mean in black, ensemble standard deviation in gray). (h) PDF of CWV for SSTs of 300- and 304-K SST, averaged from Days 85 to 100. The dots denote the 88th percentile.

BLW_C value of about 0.9. In the presented analysis, we applied a 2-day running mean to the CWV field to filter short-lived convective cells.

Finally, it is interesting to compare the time evolution of BLW with the time evolution of the interquartile range (IQR) of CWV (75th to 25th percentile)—a widely used, PDF-based index for assessing self-aggregation in simulations (e.g., Arnold & Randall, 2015; Bretherton et al., 2005; Holloway & Woolnough, 2016; C. J. Muller & Held, 2012). As increasing values of IQR indicate an increase in the degree of aggregation, the time evolution of IQR (Figure 4f) alone would suggest that the simulation already reaches its fully aggregated state after about 20 days. IQR can be shown to mainly capture the evolution of the dry mode, hence missing essential parts of the aggregation process (see Figures 4a–4e), which are well captured by BLW_C. We find similar shortcomings when contrasting how BLW and the IQR of column relative humidity change with SST in Appendix C.

4.3. Reanalysis of the Atlantic ITCZ

In its stripe version (BLW_S), the BLW index provides a tool to assess the evolution of the CWV field in the tropical Atlantic while yielding values comparable to BLW_C used for the RCE simulations. Below, we illustrate these capabilities by extracting the seasonal cycle of aggregation of the Atlantic ITCZ using the 83rd percentile of CWV to define the moist margin.

The seasonal cycle of BLW_S exhibits two minima indicating two periods during which the Atlantic ITCZ is in a comparatively disaggregated state, one during boreal spring (local minimum on 16 March) and one during boreal fall (local minimum on 16 September); see Figure 5. To obtain the BLW_S climatology, the index has been computed on the hourly CWV snapshots of the ERA5 reanalysis and then binned into biweekly intervals. In spring, the BLW_S reaches lower values because the CWV field frequently develops a second band of high humidity values located in the southwestern part of the domain (see, e.g., 1 May in Figure 5b) whereas in summer it is more common to have a single band (see, e.g., 20 June). The lower values of BLW_S in the fall are associated with the moist margin being regularly disturbed toward the North (see, e.g., 9 September).
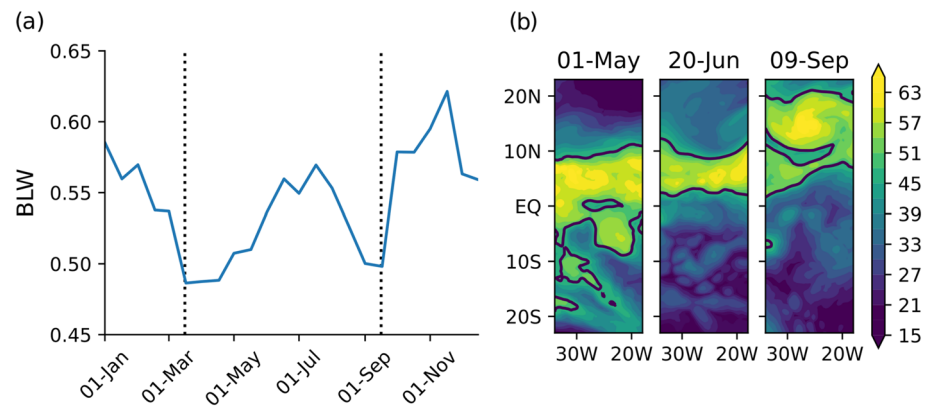
Figure 5. (a) The annual cycle of BLW_S diagnosed for the 2000–2017 period. The two dotted lines mark 16 March and 16 September. (b) Snapshots of CWV for 3 days in 2010, representing the Atlantic ITCZ's annual cycle.

During boreal spring, the low values of BLW_S agree with previous studies which show that high variability in moisture and precipitation is common during this time of year (see also Figure 1 in Chiang et al., 2002). A possible explanation for the increase in variability in the CWV distribution is that the ITCZ, delimited by the moist margin, approaches its southernmost extent. As a consequence, land-ocean interactions with the South American Continent might impact the shape of the CWV distribution. An alternative explanation might be that the weaker SST gradient during this time of year more weakly constrains the location of the ITCZ. Low values of BLW_S during boreal fall may come from the moist margin's distortion by African Easterly Waves and Hurricanes (peak season in mid-September, see, e.g., Landsea, 1993). In particular, the CWV fields with low values of BLW_S in the fall often show moist filaments extending toward the north, that is, into the previously dry regions, and dry filaments extending toward the south, that is, into the previously moist region, in a whirl-like pattern.

5. Conclusion

In conclusion, the length of the moist tropical margin (MML) can quantify convective aggregation in both idealized simulations and realistic data of the tropical atmosphere: The shorter the MML, the more aggregated the atmosphere. We have shown that:

1. The moist margin is well identified using the antimode of the CWV distribution and easy to visualize (Figure 1).
2. The MML is linked to the evolution of the entire CWV distribution via the system's Gibbs free energy (Figure 2).
3. This allows us to formulate a robust index (BLW) to quantify convective aggregation across data sets and geometries (Figure 3).
4. Unlike traditional aggregation metrics, BLW can track both the coalescence and coarsening of moist regions across a wide range of climates despite only requiring the choice of a fixed CWV percentile (Figure 4).
5. BLW quantifies aggregation in realistic data sets, as shown by its ability to quantify the seasonal cycle of the Atlantic ITCZ's organization (Figure 5).

Compared to other convective organization indices such as SCAI (Tobin et al., 2012), COP (White et al., 2018), or Iorg (Tompkins & Semie, 2017), BLW is easy to interpret as the moist margin can be superimposed on the moisture field. Furthermore, BLW only relies on two transparent choices: (1) the fixed percentile defining the moist margin and (2) the reference underlying shape of the moisture field. Both choices have default values facilitating the calculation of BLW: (1) The percentile can be chosen as the antimode of the CWV PDF if it is bimodal or as the maximum of the CWV PDF if it is unimodal; and (2) the reference underlying shape can be chosen as a circle for large square domains or as a band for elongated domains with anisotropic surface conditions. Compared to other shape-based organization indices (e.g., MacEachren, 1985; Pscheidt et al., 2019), BLW is strongly rooted in theory as we have shown in

section 3.4 that the MML is closely related to the empirically determined Gibbs free energy of the system. This link, analogous to surface tension, allows us to relate BLW to the physical processes driving the evolution of the moisture field, hence opening the door to simple theories for the bimodal distribution of tropical water vapor (e.g., Masunaga & Mapes, 2020). Note that we have focused on CWV rather than MSE for consistency with the moist margin's literature: As the CWV budget is dominated by advection, precipitation, and evaporation, it makes the potential's shape hard to predict a priori, possibly reducing it to a diagnostic tool. Using MSE allows us to bypass this limitation by decomposing the potential into diabatic components that can be individually interpreted, as we show in Appendix B.

For conciseness, we have made several limiting choices throughout the manuscript. First, we have limited ourselves to the COSMO model for idealized RCE simulations because it leverages graphics processing units (GPUs) to run large ensembles on big domains at high resolution (see Appendix A). While we have anecdotal evidence that the MML can successfully quantify convective organization in RCE simulations using different models (e.g., models from Wing et al., 2018), BLW should be compared to other indices across models to test its broad applicability. Here, we have purposely avoided tuning BLW for intercomparison purposes to keep a strong link with theory. Second, we have quantified organization in idealized simulations and reanalysis of different geometries to show the versatility of the moist margin's approach. However, this limits our ability to meaningfully compare idealized simulations to observations, as, for example, idealized simulations with weak rotation and meridional surface temperature gradients would be better analogs to the Atlantic ITCZ (e.g., Müller & Hohenegger, 2020).

Overall, our work generalizes the coarsening theory of Windmiller and Craig (2019) to develop a mixed Eulerian-Lagrangian framework that simplifies (dis)aggregation processes to a competition between two opposing tendencies: (1) aggregating tendencies that typically show a double-well potential structure and effectively act as a surface tension for the moist margin and (2) disaggregating tendencies that typically show a single-well potential structure and stretch or break the moist margin. Exciting opportunities lie ahead, such as evaluating this effective surface tension as an emergent constraint for the behavior of convective parametrizations and using BLW to study the effect of aggregation on precipitation and climate sensitivity in atmospheric observations (e.g., Popp & Bony, 2019).

Appendix A: Three-Dimensional RCE Simulations

The simulations were performed with the nonhydrostatic limited-area weather and climate model COSMO (Consortium for Small-scale Modeling model, v5.0, Steppeler et al., 2003). In this model the thermo-hydrodynamical Euler equations are discretized on a structured longitude-latitude-height mesh using finite difference methods. The discretization schemes include a fifth-order upwind scheme for horizontal advection (Baldauf et al., 2011) and a split-explicit three-stage second-order Runge-Kutta time-stepping scheme for the forward integration in time (Wicker & Skamarock, 2002). To damp gravity waves at the upper boundary, an implicit Rayleigh damping term on the vertical velocity is added at the end of each acoustic time step (Klemp et al., 2008).

Subgrid-scale processes include an interactive radiative transfer scheme based on the δ-two-stream approach (Ritter & Geleyn, 1992) and a single-moment bulk cloud-microphysics scheme with five hydrometeor species (cloud water, cloud ice, rain, snow, and graupel, Reinhardt & Seifert, 2005). In the planetary boundary layer and for surface transfer, a turbulent-kinetic-energy-based parameterization is used (Mellor & Yamada, 1982; Raschendorfer, 2001), and parametrizations for convection have been switched off.

The presented set of simulations have become possible due to a new version of COSMO capable of exploiting accelerators based on graphics processing units (GPUs), which possess properties beneficial for weather and climate codes (Fuhrer et al., 2014; Owens et al., 2008). Our version supports executing the entire time stepping on GPU accelerators and thus avoids expensive data movements between host CPU and GPU accelerators. In practice, these capabilities enable kilometer-resolution simulations on near-global computational domains over extended periods of time (Fuhrer et al., 2018; Leutwyler et al., 2016; Leutwyler & Schär, 2019). Here we exploit the capabilities to obtain a set of cloud-resolving RCE simulations at nine different sea surface temperatures (SSTs).

For the GPU version of COSMO, extensive validation has been conducted for kilometer-scale configurations. Examples include a 10-year-long reanalysis-driven simulation over Europe (Leutwyler et al., 2018),

validation of clouds (Hentgen et al., 2019), and surface winds (Belušić et al., 2018). Note that in our version of the COSMO model the atmospheric moisture budget is not strictly conserved. In the equilibrium phase of the simulation (last 40 days) about $0.069\,\mathrm{kg\,m^{-2}\,day^{-1}}$ of water is lost, that is, about 1.5% of the latent heat flux.

Appendix B: Decomposition of the Potential Into Diabatic Tendencies and Advection

In this section, we choose column frozen moist static energy (MSE for short, in units $\mathrm{W\,m^{-2}}$) as our order variable to decompose the potential into contributions from diabatic tendencies and MSE advection. Our starting point is the budget for column MSE, which we write in Eulerian form:

$$\frac{\partial \mathrm{MSE}}{\partial t} = \sum_{i\,=\,\mathrm{lw,\,sw,\,sef,\,adv}} \dot{\mathrm{MSE}}_i = - \sum_{i\,=\,\mathrm{lw,\,sw,\,sef,\,adv}} \frac{dV_i(\mathrm{MSE})}{d\mathrm{MSE}}, \tag{B1}$$

where we have decomposed the MSE tendency into its contribution from the net longwave atmospheric heating (lw), the net shortwave atmospheric heating (sw), the surface enthalpy fluxes (sef), and the horizontal flux of MSE (adv, here calculated as a residual) through the grid cell's boundaries. We calculate a potential for each tendency using Equation 3 and depict the results in Figure B1.

The first step is to redefine the moist margin to accommodate the change from CWV to MSE, which we do using the antimode of the MSE PDF for consistency with section 3. For the 300-K idealized RCE simulation (Figure B1a), we identify the antimode as the 88th percentile of the MSE PDF (Figure B1c), which is the same as the percentile chosen for CWV (Figure 2a) and underlines the strong constraint on weak temperature gradients in nonrotating RCE (e.g., Sobel & Bretherton, 2000). In contrast, for the tropical Atlantic reanalysis (Figure B1b), the MSE PDF (Figure B1d) is quite different from the CWV PDF (Figure 2b) and only marginally bimodal on the most aggregated day (4 December), whose antimode corresponds to the 67th percentile.

If the potential is directly decomposed using Equation 2, the total potential is an order of magnitude smaller than its individual components. As a consequence, Figures B1e and B1f highlight the well-known atmospheric energy balance to first order: For instance, the atmosphere cools to space via longwave radiation, resulting in a negative tendency, which translates to a positive slope that tries to reduce atmospheric MSE. This order-of-magnitude difference between the total potential and its individual contributions suggests that *anomalies* from the atmospheric energy balance are responsible for the double-well shape of the total potential. This motivates investigating the budget for the spatial anomaly of MSE:

$$\frac{\partial \mathrm{MSE}'}{\partial t} = \sum_{i\,=\,\mathrm{lw,\,sw,\,sef,\,adv}} \dot{\mathrm{MSE}}'_i = - \sum_{i\,=\,\mathrm{lw,\,sw,\,sef,\,adv}} \frac{dV'_i(\mathrm{MSE})}{d\mathrm{MSE}}, \tag{B2}$$

where we have introduced the spatial anomaly $X' \stackrel{\mathrm{def}}{=} X - \langle X \rangle_{\mathscr{D}}$ from the domain-average $\langle X \rangle_{\mathscr{D}}$ of a variable X. Note that Equation B2 is derived by taking the spatial anomaly of Equation B1 without assuming that the domain-mean MSE is steady. This assumption does not hold in our case, leading to a difference between the total potential derived from the MSE anomaly (dotted black line in Figures B1g and B1h) and the total potential derived from the total MSE (full black line). As both potentials are similar and exhibit a double-well structure, we proceed to analyze how individual components of the potential derived from MSE anomalies, which are now of the same order of magnitude as the total potential, sum up to a double-well structure. First, the "walls" of the potential for extreme MSE values come from the advection term, which smoothes out the largest MSE anomalies through overturning circulations (e.g., Holloway & Woolnough, 2016). The "moist well" comes from the decrease in longwave cooling at high CWV values (e.g., Beucler & Cronin, 2016), which heats the moist regions and effectively moistens them because of weak buoyancy gradients. The "dry well" comes from both the increase in longwave cooling and the decrease in anomalous shortwave heating at low CWV values. Finally, surface enthalpy fluxes oppose the double-well tendency by damping near-surface enthalpy disequilibrium, favoring a single-well potential and hence a unimodal MSE distribution. Overall, both idealized RCE simulations and observations offer a consistent picture of the anomalous MSE tendencies responsible for the double-well potential
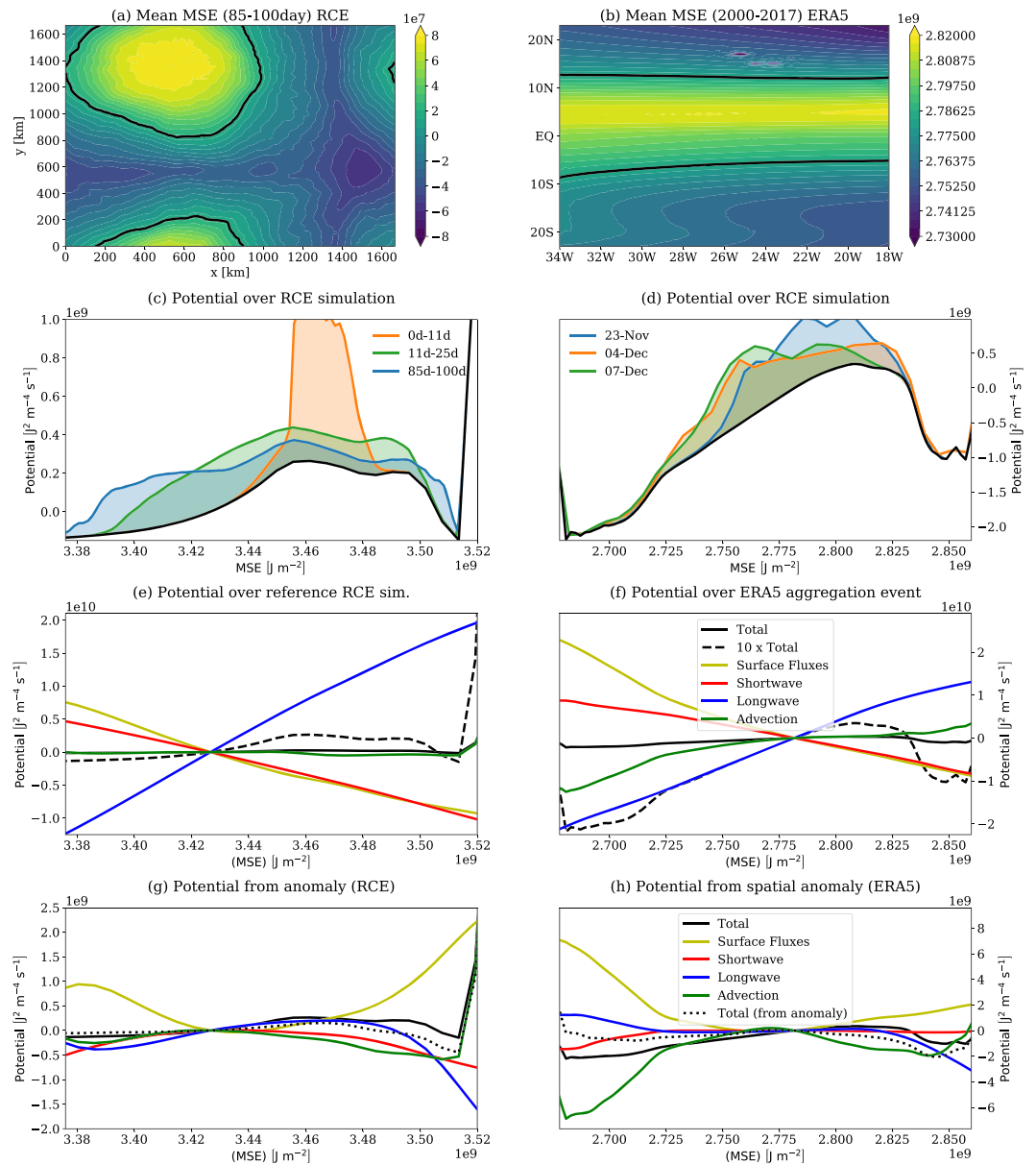
Figure B1. (a) Time-mean MSE field in RCE for Days 85–100 with the 88th percentile marked in black. (b) Time-mean MSE field in ERA5 over 2000–2017 with the 67th percentile marked in black. (c) Potential for MSE calculated over the RCE simulation (black line), where we have added the scaled PDFs of MSE for different times using colored lines and shading. (d) Potential for MSE calculated between 23 November and 4 December (black line), where we have added the scaled PDFs of MSE for different days using colored lines and shading. (e) Potential calculated for each term of Equation B1 for RCE. (f) Potential calculated for each term of Equation B1 for ERA5. (g) Potential calculated for each term of Equation B2 for RCE. (h) Potential calculated for each term of Equation B2 for ERA5.

structure. The main difference is a larger double-well potential for MSE advection in ERA5, which is expected as the Atlantic ITCZ is out of balance but requires further work as the MSE budget is not explicitly closed in ERA5 reanalysis.

Appendix C: Defining BLW Across Climates

Applying the BLW index entails choosing the idealized equilibrium shape of the moist region and choosing a CWV contour representative of the potential hill separating the two potential wells. The choice of a contour can be intricate as the different modes of the CWV distribution can change with SST (see Figure C1) and
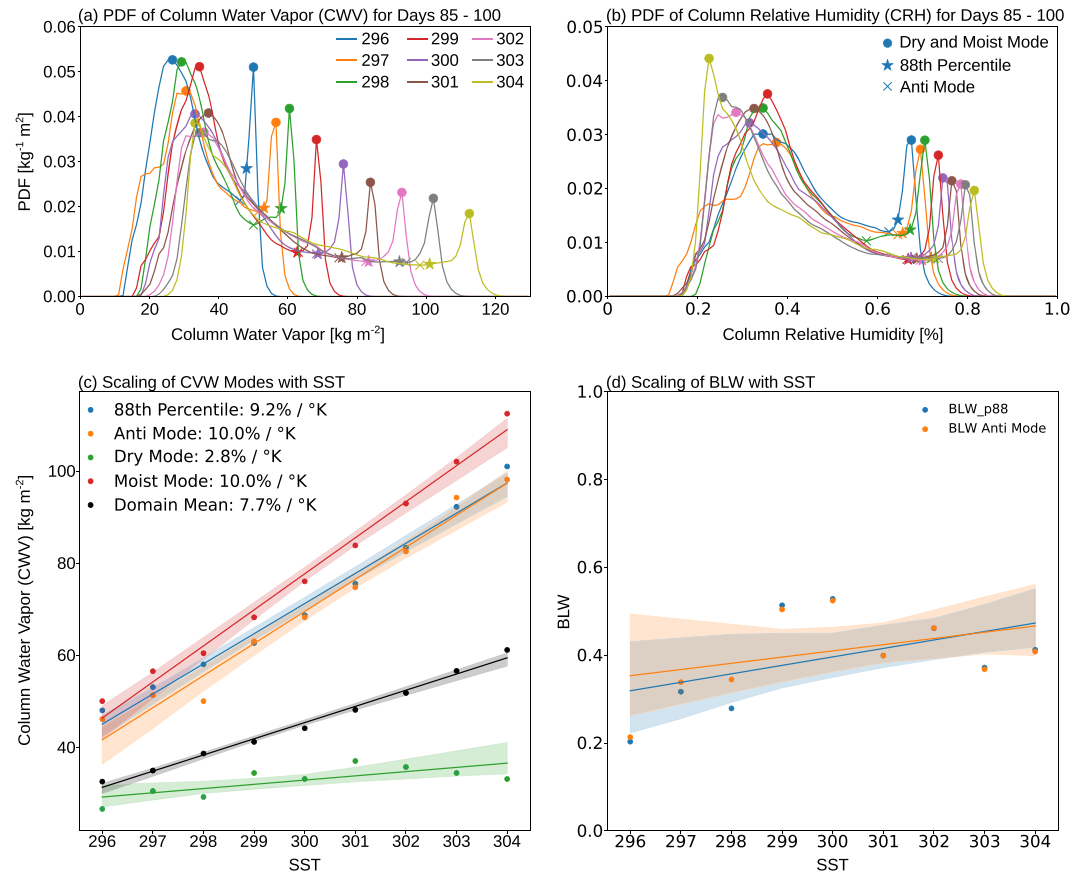
Figure C1. Scaling of CWV distribution modes with SST for the last 15 days of the RCE simulations. (a) CWV PDF at different SSTs (colored lines). The colored markers indicate the dry and moist local maxima (dots), the local minimum of the antimode (cross), and the 88th percentile (star). (b) Same as (a), but for column relative humidity. (c) Scaling of the modes with SST. The solid lines represent the scaling using the mean slope (also indicated in the upper-left corner), and the shading the scaling using the 5th and 95th percentiles of the slope. The slope estimates were obtained by randomly choosing (with replacement) from the nine SST samples. (d) Same as (b), but for the final BLW_C index. We use two different thresholds to define MML: The 88th percentile (blue dots) or the local minimum separating the two local maxima of the PDF (orange dots).

because the antimode of the CWV distribution is not always well defined. For example, the PDF's antimode is ill defined when the CWV distribution exhibits multiple local minima (see, e.g., green line in Figure C1a). For ERA5, a similar problem arises, since the CWV distribution occasionally becomes unimodal (Figure 1), making an index based on the local minimum undefined.

To address this issue, we adopt a definition based on a temporally fixed percentile of CWV, meaning that the domain is split into a moist and a dry region with temporally fixed areas. Motivated by the study of Jakob et al. (2019), the 88th percentile of CWV (wet-dry ratio of about 1:9) was chosen for the RCE simulation. For the Atlantic ITCZ, the 83rd percentile of CWV (ratio of about 1:6) was chosen, since it corresponds to the $48\,\mathrm{kg\,m^{-2}}$ contour proposed by Mapes et al. (2018). We discuss below the robustness of using the 88th percentile of CWV to represent the antimode for RCE.

The 88th percentile of CWV tracks the minimum of the CWV PDF reasonably well across a range of SSTs (Figures C1 and 1c). For the equilibrium phase (Days 85–100), the contour is akin to the minimum at an SST of 299–304 K, while it resides on the hillside of the moist mode for colder SSTs (296 and 298 K). While the match between the minimum and 88th percentile is not perfect, the two indices scale approximately at the same rate with SST ($9.2\%\,\mathrm{K^{-1}}$ and $10\%\,\mathrm{K^{-1}}$). That rate is faster than that of the mean CWV ($7.7\%\,\mathrm{K^{-1}}$) or the dry mode ($2.8\%\,\mathrm{K^{-1}}$) and also matches that of the moist mode ($10\%\,\mathrm{K^{-1}}$). Note that the

differential scaling of the two modes leads to a less sharp MML at warmer SSTs, since the valley separating the two maxima becomes wider.

The shape of the CWV distribution provides first indication of the organization in the RCE simulations. For instance, the distance between the marker of the 88th percentile (star) and the line of zero PDF (*x*-axis) is representative of the MML. The analysis presented in Figure C1 indicates that the MML is slightly longer at cold SSTs (296–298 K) but remains almost at the same length for SSTs between 299 and 304 K. In practice, the difference between the three cold simulations and the remaining set emerges from the number of clusters. In the colder simulations, we detect two clusters, while we find only one in the warmer simulations. It is thus only in the warm simulations that variations in BLW describe how the final cluster approaches a circular shape. Based on BLW, the 299- and 300-K simulations can be considered the most organized.

The geometrical perspective of the BLW index gives additional information compared to established aggregation indices. For instance, the popular IQR metric applied to column relative humidity would suggest that warmer simulations are more organized because their IQR is larger (Figure C1b). This can also be seen by looking at the CWV PDF (Figure C1a), where the dry mode moves to the left and the moist mode moves to the right. In contrast, the geometric perspective of BLW suggests little to no change in aggregation with warming (Figure C1d) as convection clusters in a more circular shape at SST = 300 K than at SST = 304 K despite the increase in column relative humidity variance at 304 K.

Appendix D: Potential and MML Timescales

In this section, our goal is to estimate (1) the timescale to reach local equilibrium (fast formation of small-scale moist and dry regions) and (2) the timescale to reach global equilibrium in RCE (slow formation of a single moist cluster, Figure 1a) and to form the "ITCZ stripe" in ERA5 (Figure 1b). The timescale of local equilibrium (τ_{MML}) corresponds to fast time variations of the MML defined in section 3.4, while the timescale of global equilibrium (τ_V) is governed by the empirical potential defined in section 3.2. In the absence of an exact theory, we diagnose both timescales from data and require that the timescales minimally depend on the spatiotemporal resolution of each data set and describe the nonmonotonic oscillations of the observed MML.

To estimate the MML timescale, we choose the e-folding timescale of the autocorrelation function, defined as the inverse Fourier transform of the MML's temporal power spectrum (e.g., section 8.10 of Dunn, 2005). The autocorrelation function of the MML, depicted in Figure D1a for RCE and Figure D1b for ERA5, is normalized by its maximum to yield values between −1 and 1. We put uncertainty bounds on the e-folding
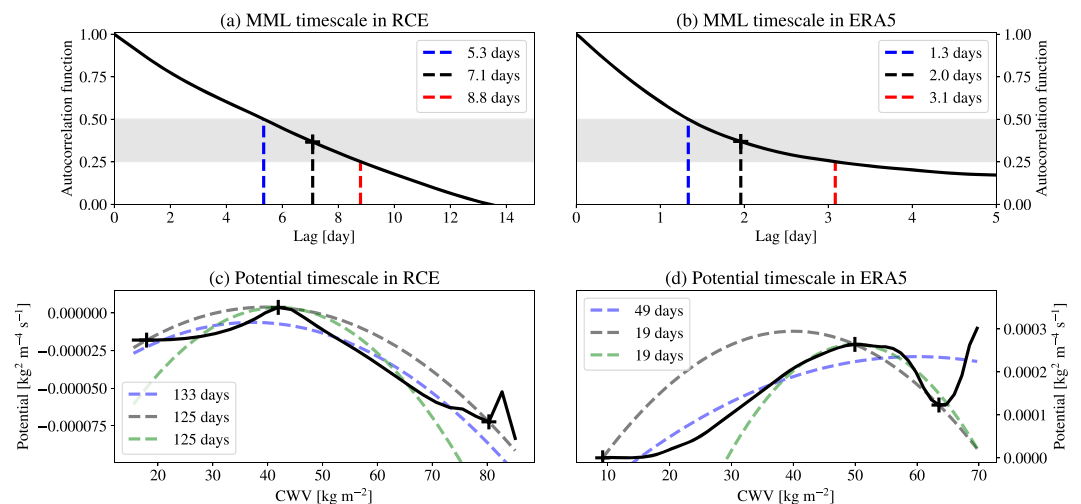

Figure D1. Three estimates of the MML timescale (vertical dashed lines) using the normalized autocorrelation function (black line) for RCE (panel a) and ERA5 (panel b). Three estimates of the potential timescale using Equation D2 and three polynomial approximations (dashed lines) for the potential (full black line) for RCE (panel c) and ERA5 (panel d).

timescale τ_{MML} by additionally finding the shortest lag for which the normalized autocorrelation function is 0.5 and 0.25, leading to estimates of $\tau_{\text{MML}} = (7.1 \pm 1.8)$days for RCE and $\tau_{\text{MML}} = (2.0 \pm 1.1)$days for ERA5.

To estimate the potential timescale, we linearize the time evolution Equation 2 about the CWV value CWV_{max} where the potential reaches its maximal value V_{max}:

$$\frac{\partial \text{CWV}}{\partial t} \approx -\left(\frac{d^2 V}{d\text{CWV}^2}\right)_{\text{CWV}_{\text{max}}} \times (\text{CWV} - \text{CWV}_{\text{max}}). \tag{D1}$$

Equation D1 describes a scenario where an initially uniform CWV field of intermediate CWV value CWV_{max}, subjected to the bimodal potential V with local minima $V_1 \overset{\text{def}}{=} V(\text{CWV}_1)$ and $V_2 \overset{\text{def}}{=} V(\text{CWV}_2)$, evolves toward a self-aggregated state. The linear timescale dictating the evolution of CWV is given by the inverse of the potential's second derivative evaluated at CWV_{max}:

$$\tau_V \overset{\text{def}}{=} -\left(\frac{d^2 V}{d\text{CWV}^2}\right)^{-1}_{\text{CWV}_{\text{max}}}. \tag{D2}$$

To calculate τ_V from Equation D2, we estimate the second derivative of V using three different methods for robustness:

1. We fit a second-order polynomial (dashed blue lines in Figure D1) using all potential values between CWV_1 and CWV_2 (the left and right black crosses in Figure D1) and estimate τ_V from its leading coefficient.
2. We fit a second-order polynomial (dashed gray lines in Figure D1) using the three local extrema of the potential function (black crosses in Figure D1) and estimate τ_V from its leading coefficient.
3. We approximate the local curvature of the potential V (dashed green lines in Figure D1) using a second-order Taylor-Series expansion at CWV_1, CWV_{max}, and CWV_2, from which we estimate τ_V.

Reassuringly, the mathematically equivalent second and third methods give the same results to good precision, while the first method gives an upper bound for τ_V, leading to estimates of $\tau_V = (125$–$133)$ days for RCE and $\tau_V = (19$–$49)$ days for ERA5.

We can now estimate the ratio of the short timescale τ_{MML} to the long timescale τ_V: $\tau_{\text{MML}}/\tau_V \approx (4$–$7)\%$ for RCE and $\tau_{\text{MML}}/\tau_V \approx (3$–$16)\%$ for ERA5. This confirms that the timescales of local and global equilibria are separated by 1 to 2 orders of magnitude for both data sets, despite the real tropics evolving approximately five times faster than RCE.

Data Availability Statement

The Github repository for our project can be found at https://github.com/tbeucler/2019_WMI (http://hdl.handle.net/21.11116/0000-0006-EC6A-A). The particular version of the COSMO model used in this study is based on the official version 5.0 with many additions to enable GPU capability and available under a license (https://www.cosmo-model.org/content/consortium/licencing.htm). The ERA5 reanalysis data set, provided by the Copernicus Climate Change Service (C3S), was directly downloaded from the Copernicus Climate Change Service Climate Data Store (CDS, https://cds.climate.copernicus.eu/cdsapp#!/home) in October 2018 on the Engaging computing cluster provided by MIT before being copied over to CSCS.

References

Arnold, N. P., & Randall, D. A. (2015). Global-scale convective aggregation: Implications for the Madden-Julian oscillation. *Journal of Advances in Modeling Earth Systems*, *7*, 1499–1518. https://doi.org/10.1002/2015MS000498

Baldauf, M., Seifert, A., Förstner, J., Majewski, D., Raschendorfer, M., & Reinhardt, T. (2011). Operational convective-scale numerical weather prediction with the COSMO model: Description and sensitivities. *Monthly Weather Review*, *139*(12), 3887–3905. https://doi.org/10.1175/MWR-D-10-05013.1

Belušić, A., Prtenjak, M. T., Güttler, I., Ban, N., Leutwyler, D., & Schär, C. (2018). Near-surface wind variability over the broader Adriatic region: Insights from an ensemble of regional climate models. *Climate Dynamics*, *50*(11), 4455–4480. https://doi.org/10.1007/s00382-017-3885-5

Beucler, T. (2016). A correlated stochastic model for the large-scale advection, condensation and diffusion of water vapour. *Quarterly Journal of the Royal Meteorological Society*, *142*(697), 1721–1731.

Beucler, T., Abbott, T. H., Cronin, T. W., & Pritchard, M. S. (2019). Comparing convective self-aggregation in idealized models to observed moist static energy variability near the equator. *Geophysical Research Letters*, *46*, 10,589–10,598. https://doi.org/10.1029/2019GL084130

Beucler, T., & Cronin, T. W. (2016). Moisture-radiative cooling instability. *Journal of Advances in Modeling Earth Systems*, *8*, 1620–1640. https://doi.org/10.1002/2016MS000763

Beucler, T., Cronin, T., & Emanuel, K. (2018). A linear response framework for radiative-convective instability. *Journal of Advances in Modeling Earth Systems*, *10*, 1924–1951. https://doi.org/10.1029/2018MS001280

Bretherton, C. S., Blossey, P. N., & Khairoutdinov, M. (2005). An energy-balance analysis of deep convective self-aggregation above uniform SST. *Journal of the Atmospheric Sciences*, *62*(12), 4273–4292.

Bretherton, C. S., & Sobel, A. H. (2002). A simple model of a convectively coupled walker circulation using the weak temperature gradient approximation. *Journal of climate*, *15*(20), 2907–2920.

Brogniez, H. (2004). Humidite de la troposphere libre africaine: Elaboration d'une archive meteosat, analyse climatique et evaluation de modeles, Université Pierre et Marie Curie-Paris VI.

Chiang, J. C. H., Kushnir, Y., & Giannini, A. (2002). Deconstructing Atlantic Intertropical Convergence Zone variability: Influence of the local cross-equatorial sea surface temperature gradient and remote forcing from the Eastern Equatorial Pacific. *Journal of Geophysical Research*, *107*(D1), 4004. https://doi.org/10.1029/2000JD000307

Craig, G. C. (1996). Dimensional analysis of a convecting atmosphere in equilibrium with external forcing. *Quarterly Journal of the Royal Meteorological Society*, *122*(536), 1963–1967.

Craig, G. C., & Mack, J. M. (2013). A coarsening model for self-organization of tropical convection. *Journal of Geophysical Research: Atmospheres*, *118*, 8761–8769. https://doi.org/10.1002/jgrd.50674

Dunn, P. (2005). *Measurement and data analysis for engineering and science*. Boca Raton, FL: CRC Press, Taylor & Francis Group.

Emanuel, K. (2019). Inferences from simple models of slow, convectively coupled processes. *Journal of the Atmospheric Sciences*, *76*(1), 195–208.

Emanuel, K. A., & Pierrehumbert, R. T. (1996). Microphysical and dynamical control of tropospheric water vapor. In *Clouds, chemistry and climate* (pp. 17–28). Berlin, Heidelberg: Springer.

Emanuel, K., Wing, A. A., & Vincent, E. M. (2014). Radiative-convective instability. *Journal of Advances in Modeling Earth Systems*, *6*, 75–90. https://doi.org/10.1002/2013MS000270

Fuhrer, O., Chadha, T., Hoefler, T., Kwasniewski, G., Lapillonne, X., Leutwyler, D., et al. (2018). Near-global climate simulation at 1 km resolution: Establishing a performance baseline on 4888 GPUs with COSMO 5.0. *Geoscientific Model Development*, *11*(4), 1665–1681.

Fuhrer, O., Osuna, C., Lapillonne, X., Gysi, T., Cumming, B., Arteaga, A., & Schulthess, T. C. (2014). Towards a performance portable, architecture agnostic implementation strategy for weather and climate models. *Supercomputing Frontiers and Innovations*, *1.1*, 45–62.

Held, I. M., Hemler, R. S., & Ramaswamy, V. (1993). Radiative-convective equilibrium with explicit two-dimensional moist convection. *Journal of the Atmospheric Sciences*, *50*(23), 3909–3927.

Hentgen, L., Ban, N., Krïner, N., Leutwyler, D., & Schär, C. (2019). Clouds in convection-resolving climate simulations over Europe. *Journal of Geophysical Research: Atmospheres*, *124*, 3849–3870. https://doi.org/10.1029/2018JD030150

Hersbach, H., Bell, B., Berrisford, P., Hirahara, S., Horányi, A., Muñoz Sabater, J., et al. (2020). The ERA5 global reanalysis. *Quarterly Journal of the Royal Meteorological Society*, *146*, 1999–2049. https://doi.org/10.1002/qj.3803

Holloway, C. E., & Neelin, J. D. (2009). Moisture vertical structure, column water vapor, and tropical deep convection. *Journal of the Atmospheric Sciences*, *66*, 1665–1683. https://doi.org/10.1175/2008JAS2806.1

Holloway, C. E., Wing, A. A., Bony, S., Muller, C., Masunaga, H., L'Ecuyer, T. S., et al. (2017). Observing convective aggregation. *Surveys in Geophysics*, *38*(6), 1199–1236.

Holloway, C. E., & Woolnough, S. J. (2016). The sensitivity of convective aggregation to diabatic processes in idealized radiative-convective equilibrium simulations. *Journal of Advances in Modeling Earth Systems*, *8*, 166–195. https://doi.org/10.1002/2015MS000511

Jakob, C., Singh, M. S., & Jungandreas, L. (2019). Radiative convective equilibrium and organized convection: An observational perspective. *Journal of Geophysical Research: Atmospheres*, *124*, 5418–5430. https://doi.org/10.1029/2018JD030092

Klemp, J. B., Dudhia, J., & Hassiotis, A. D. (2008). An upper gravity-wave absorbing layer for NWP applications. *Monthly Weather Review*, *136*(10), 3987–4004. https://doi.org/10.1175/2008MWR2596.1

Krapivsky, P. L., Redner, S., & Ben-Naim, E. (2010). *A kinetic view of statistical physics*. Cambridge: Cambridge University Press. https://doi.org/10.1017/CBO9780511780516

Landsea, C. W. (1993). A climatology of intense (or major) Atlantic hurricanes. *Monthly Weather Review*, *121*, 1703–1713.

Leutwyler, D., Fuhrer, O., Lapillonne, X., Lüthi, D., & Schär, C. (2016). Towards European-scale convection-resolving climate simulations. *Geoscientific Model Development*, *2016*, 1–34.

Leutwyler, D., Lüthi, D., Ban, N., Fuhrer, O., & Schär, C. (2018). Evaluation of the convection-resolving climate modeling approach on continental scales. *Journal of Geophysical Research: Atmospheres*, *122*, 5237–5258. https://doi.org/10.1002/2016JD026013

Leutwyler, D., & Schär, C. (2019). Barotropic instability of a cyclone core at kilometer-scale resolution. *Journal of Advances in Modeling Earth Systems*, *11*, 3390–3402. https://doi.org/10.1029/2019MS001847

Lorenz, R. D., Griffith, C. A., Lunine, J. I., McKay, C. P., & Rennò, N. O. (2005). Convective plumes and the scarcity of Titan's clouds. *Geophysical Research Letters*, *32*, L01201. https://doi.org/10.1029/2004GL021415

Müller, S. K., & Hohenegger, C. (2020). Self-aggregation of convection in spatially varying sea surface temperatures. *Journal of Advances in Modeling Earth Systems*, *12*, e2019MS001698. https://doi.org/10.1029/2019MS001698

MacEachren, A. M. (1985). Compactness of geographic shape: Comparison and evaluation of measures. *Geografiska Annaler: Series B, Human Geography*, *67*(1), 53–67.

Mapes, B. E., Chung, E. S., Hannah, W. M., Masunaga, H., Wimmers, A. J., & Velden, C. S. (2018). The meandering margin of the meteorological moist tropics. *Geophysical Research Letters*, *45*, 1177–1184. https://doi.org/10.1002/2017GL076440

Masunaga, H., & Mapes, B. E. (2020). A mechanism for the maintenance of sharp tropical margins. *Journal of the Atmospheric Sciences*, *77*, 1181–1197.

Mellor, G., & Yamada, T. (1982). Development of a turbulence closure model for geophysical fluid problems. *Reviews of Geophysics*, *20*(4), 851–875. https://doi.org/10.1029/RG020i004p00851

Minschwaner, K., & Dessler, A. E. (2004). Water vapor feedback in the tropical upper troposphere: Model results and observations. *Journal of Climate*, *17*(6), 1272–1282.

Muller, C., & Bony, S. (2015). What favors convective aggregation and why? *Geophysical Research Letters*, *42*, 5626–5634. https://doi.org/10.1002/2015GL064260

Muller, C. J., & Held, I. M. (2012). Detailed investigation of the self-aggregation of convection in cloud-resolving simulations. *Journal of the Atmospheric Sciences*, *69*(8), 2551–2565.

Owens, J. D., Houston, M., Luebke, D., Green, S., Stone, J. E., & Phillips, J. C. (2008). GPU computing. *Proceedings of the IEEE*, *96*(5), 879–899. https://doi.org/10.1109/JPROC.2008.917757

Parsons, D. B., Yoneyama, K., & Redelsperger, J.-L. (2000). The evolution of the tropical western Pacific atmosphere-ocean system following the arrival of a dry intrusion. *Quarterly Journal of the Royal Meteorological Society*, *126*, 517–548. https://doi.org/10.1002/qj.49712656307

Patrizio, C. R., & Randall, D. A. (2019). Sensitivity of convective self-aggregation to domain size. *Journal of Advances in Modeling Earth Systems*, *11*, 1995–2019. https://doi.org/10.1029/2019MS001672

Peters, O., Neelin, J. D., & Nesbitt, S. W. (2009). Mesoscale convective systems and critical clusters. *Journal of the Atmospheric Sciences*, *66*(9), 2913–2924.

Pierrehumbert, R. T., Brogniez, H., & Roca, R. (2007). *On the relative humidity of the Earth's atmosphere*. Princeton, NJ: Princeton University Press.

Pierrehumbert, R. T., & Roca, R. (1998). Evidence for control of Atlantic subtropical humidity by large scale advection. *Geophysical Research Letters*, *25*(24), 4537–4540.

Popp, M., & Bony, S. (2019). Stronger zonal convective clustering associated with a wider tropical rain belt. *Nature Communications*, *10.1*, 1–12.

Posselt, D. J., Heever, S. v. d., Stephens, G., & Igel, M. R. (2012). Changes in the interaction between tropical convection, radiation, and the large-scale circulation in a warming environment. *Journal of Climate*, *25*(2), 557–571.

Pscheidt, I., Senf, F., Heinze, R., Deneke, H., Trömel, S., & Hohenegger, C. (2019). How organized is deep convection over Germany? *Quarterly Journal of the Royal Meteorological Society*, *145*(723), 2366–2384.

Raschendorfer, M. (2001). The new turbulence parameterization of LM. Model Development and Application, COSMO Newsletter, No. 1, available online at http://www.cosmo-model.org/content/model/documentation/newsLetters/newsLetter/newsLetter_01.pdf

Redelsperger, J.-L., Parsons, D. B., & Guichard, F. (2002). Recovery processes and factors limiting cloud-top height following the arrival of a dry intrusion observed during TOGA COARE. *Journal of the Atmospheric Sciences*, *59*, 2438–2457. https://doi.org/10.1175/1520-0469(2002)059<2438:RPAFLC>2.0.CO;2

Reinhardt, T., & Seifert, A. (2005). A three-category ice-scheme for LMK. Model Development and Application, COSMO Newsletter, No. 6, available online at http://www.cosmomodel.org/content/model/documentation/newsLetters/newsLetter06/cnl6_reinhardt.pdf).

Rennó, N. O., & Ingersoll, A. P. (1996). Natural convection as a heat engine: A theory for CAPE. *Journal of the Atmospheric Sciences*, *53*(4), 572–585. https://doi.org/10.1175/1520-0469(1996)053<0572:NCAAHE>2.0.CO;2

Ritter, B., & Geleyn, J. F. (1992). A comprehensive radiation scheme for numerical weather prediction models with potential applications in climate simulations. *Monthly Weather Review*, *120*, 303–325.

Robe, F. R., & Emanuel, K. A. (2001). The effect of vertical wind shear on radiative–convective equilibrium states. *Journal of the Atmospheric Sciences*, *58*(11), 1427–1445.

Rotunno, R., Klemp, J. B., & Weisman, M. L. (1988). A theory for strong, long-lived squall lines. *Journal of the Atmospheric Sciences*, *45*(3), 463–485.

Sanner, M. F., et al. (1999). Python: A programming language for software integration and development. *Journal of Molecular Graphics and Modelling*, *17*(1), 57–61.

Schroeder, D. V. (2000). *An introduction to thermal physics* (pp. 1284–1285). Reading, MA: Addison-Wesley.

Sherwood, S. C. (1996). Maintenance of the free-tropospheric tropical water vapor distribution. Part II: Simulation by large-scale advection. *Journal of Climate*, *9*(11), 2919–2934.

Sherwood, S. C. (1999). Convective precursors and predictability in the tropical western Pacific. *Monthly Weather Review*, *127*(12), 2977–2991.

Sherwood, S. C., Kursinski, E. R., & Read, W. G. (2006). A distribution law for free-tropospheric relative humidity. *Journal of climate*, *19*(24), 6267–6277.

Sobel, A. H., & Bretherton, C. S. (2000). Modeling tropical precipitation in a single column. *Journal of Climate*, *13*(24), 4378–4392.

Soden, B. J., & Bretherton, F. P. (1993). Upper tropospheric relative humidity from the goes 6.7 μm channel: Method and climatology for July 1987. *Journal of Geophysical Research*, *98*(D9), 16,669–16,688.

Steppeler, J., Doms, G., Schättler, U., Bitzer, H. W., Gassmann, A., Damrath, U., & Gregoric, G. (2003). Meso-gamma scale forecasts using the nonhydrostatic model LM. *Meteorology and Atmospheric Physics*, *82*(1–4), 75–96.

Sun, D.-Z., & Lindzen, R. S. (1993). Distribution of tropical tropospheric water vapor. *Journal of the Atmospheric Sciences*, *50*(12), 1643–1660.

Tobin, I., Bony, S., & Roca, R. (2012). Observational evidence for relationships between the degree of aggregation of deep convection, water vapor, surface fluxes, and radiation. *Journal of Climate*, *25*(20), 6885–6904.

Tompkins, A. M. (2001). Organization of tropical convection in low vertical wind shears: The role of water vapor. *Journal of the Atmospheric Sciences*, *58*, 529–545 EN. https://doi.org/10.1175/1520-0469(2001)058<0529:OOTCIL>2.0.CO;2

Tompkins, A. M., & Craig, G. C. (1998). Radiative–convective equilibrium in a three-dimensional cloud-ensemble model. *Quarterly Journal of the Royal Meteorological Society*, *124*(550), 2073–2097.

Tompkins, A. M., & Semie, A. G. (2017). Organization of tropical convection in low vertical wind shears: Role of updraft entrainment. *Journal of Advances in Modeling Earth Systems*, *9*, 1046–1068. https://doi.org/10.1002/2016MS000802

Van der Walt, S., Schönberger, J. L., Nunez-Iglesias, J., Boulogne, F., Warner, J. D., Yager, N., et al. (2014). scikit-image: Image processing in Python. *PeerJ*, *2*, e453.

White, B. A., Buchanan, A. M., Birch, C. E., Stier, P., & Pearson, K. J. (2018). Quantifying the effects of horizontal grid length and parameterized convection on the degree of convective organization using a metric of the potential for convective interaction. *Journal of the Atmospheric Sciences*, *75*(2), 425–450.

Wicker, L., & Skamarock, W. (2002). Time-splitting methods for elastic models using forward time schemes. *Monthly Weather Review*, *130*(8), 2088–2097.

Wimmers, A. J., & Velden, C. S. (2011). Seamless advective blending of total precipitable water retrievals from polar-orbiting satellites. *Journal of Applied Meteorology and Climatology*, *50*(5), 1024–1036.

Windmiller, J. M., & Craig, G. C. (2019). Universality in the spatial evolution of self-aggregation of tropical convection. *Journal of the Atmospheric Sciences*, *76*(6), 1677–1696.

Wing, A. A., & Cronin, T. W. (2016). Self-aggregation of convection in long channel geometry. *Quarterly Journal of the Royal Meteorological Society*, *142*(694), 1–15.

Wing, A. A., & Emanuel, K. A. (2014). Physical mechanisms controlling self-aggregation of convection in idealized numerical modeling simulations. *Journal of Advances in Modeling Earth Systems*, *6*, 59–74. https://doi.org/10.1002/2013MS000269

Wing, A. A., Emanuel, K., Holloway, C. E., & Muller, C. (2017). Convective self-aggregation in numerical simulations: A review. In *Shallow clouds, water vapor, circulation, and climate sensitivity* (pp. 1–25). Cham: Springer.

Wing, A. A., Reed, K. A., Satoh, M., Stevens, B., Bony, S., & Ohno, T. (2018). Radiative-convective equilibrium model intercomparison project. *Geoscientific Model Development*, *11*(2), 793–813. https://doi.org/10.5194/gmd-11-793-2018

Yang, H., & Pierrehumbert, R. T. (1994). Production of dry air by isentropic mixing. *Journal of the Atmospheric Sciences*, *51*(23), 3437–3454.

Zhang, C., Mapes, B. E., & Soden, B. J. (2003). Bimodality in tropical water vapour. *Quarterly Journal of the Royal Meteorological Society: A Journal of the Atmospheric Sciences, Applied Meteorology and Physical Oceanography*, *129*(594), 2847–2866.